

Deep neural operators can predict the real-time response of floating offshore structures under irregular waves

Qianying Cao^{a,b}, Somdatta Goswami^b, George Em Karniadakis^{b,c,*}, Souvik Chakraborty^{d,e}

^a*State Key Lab of Coastal and Offshore Engineering, Dalian University of Technology*

^b*Division of Applied Mathematics, Brown University*

^c*School of Engineering, Brown University*

^d*Department of Applied Mechanics, Indian Institute of Technology Delhi*

^e*School of Artificial Intelligence, Indian Institute of Technology Delhi*

Abstract

The use of neural operators in a digital twin model of an offshore floating structure can provide a paradigm shift in structural response prediction and health monitoring, providing valuable information for real-time control. In this work, the performance of three neural operators is evaluated, namely, deep operator network (DeepONet), Fourier neural operator (FNO), and Wavelet neural operator (WNO). We investigate the effectiveness of the operators to accurately capture the responses of a floating structure under six different sea state codes (3 – 8) based on the wave characteristics described by the World Meteorological Organization (WMO). The results demonstrate that these high-precision neural operators can deliver structural responses more efficiently, up to two orders of magnitude faster than a dynamic analysis using conventional numerical solvers. Additionally, compared to gated recurrent units (GRUs), a commonly used recurrent neural network for time-series estimation, neural operators are both more accurate and efficient, especially in situations with limited data availability. To further enhance the accuracy, novel extensions, such as wavelet-DeepONet and self-adaptive WNO, are proposed. Taken together, our study shows that FNO outperforms all other operators for approximating the mapping of one input functional space to the output space as well as for responses that have small bandwidth of the frequency spectrum, whereas for learning the mapping of multiple functions in the input space to the output space as well as for capturing responses within a large frequency spectrum, DeepONet with historical states provides the highest accuracy.

Keywords: neural operators, floating offshore structures, irregular wave

1. Introduction

Deep-water explorations are being pushed into harsher environments due to rising resource and energy demands. There is a pressing need for offshore floating structures that are safe and reliable since structural failure in deep water may result in significant economic and environmental damage. In deep water, floating structures can move in six degrees of freedom (DOFs) when stimulated by environmental forces, but their position is restricted by mooring systems. Computing the response

*Corresponding author.

Email addresses: qianying_cao@brown.edu (Qianying Cao), somdatta_goswami@brown.edu (Somdatta Goswami), george_karniadakis@brown.edu (George Em Karniadakis), souvik@am.iitd.ac.in (Souvik Chakraborty)

of floating structures under incident waves is challenging. The response characteristics, such as the nonlinearity, the wide-band spectrum, and the multi-scale features, are exceedingly complex. For example, the surge motion of a semi-submersible platform usually consists of wave frequency and low-frequency (slow-drift) parts, whose periods have different scales in time [1]. Motions in the six DOFs of the platform and the tensions of mooring lines constitute a significant challenge to carry out offshore work. Accurate response prediction becomes crucial given the aforementioned constraints.

Data-driven machine learning algorithms like dynamic mode decomposition [2], sparse identification for nonlinear dynamics (SINDy) [3], and deep neural networks (DNNs) [4, 5] have emerged as viable and critically enabling methodologies to address the challenges of accurate predictions of complex responses for offshore floating structures [5–8], and have led to new developments in neural simulators [9–16]. Real-time response prediction usually refers to forecasting future responses within tens of seconds in real-time based on past excitation or responses. DNNs construct a vector-wise map between the past and future data based on their correlation and perform real-time prediction. For example, Guo et al. [5] predicted the heave and surge of a semi-submersible platform for 46.5s into the future by combining the LSTM cells and several fully connected layers. Furthermore, Ye et al. [6] proposed a hybrid empirical mode decomposition (EMD) model for the short-term roll and sway predictions of a semi-submersible platform. The EMD technique decomposed motion time series into a certain number of intrinsic mode functions (IMFs), and each IMF was predicted by a support vector regression model except the first IMF, which was predicted employing LSTM. Resorting to the ensemble Kalman filter algorithm, Liong and Chua [8] predicted the heave and pitch motion responses of the floating production system (FPSO) under one sea state using a three-layered feed-forward neural network (FNN). The aforementioned DNN applications are based on data correlation and could forecast responses over a time horizon of about 40 seconds into the future [13]. This short-term forecast is related to the floating structures' retardation function, which often decays to zero in seconds. One notable argument of these works is that, despite their merits for motion prediction applications, their implementations do not take physics-based information into account [7].

As pointed out previously, the second application of DNNs is for the development of neural simulators, which are analogous to the numerical software used to simulate the structural reactions to environmental excitation. Towards the development of efficient neural simulators, Christiansen et al. [9] proposed a surrogate model for computing top tensions of the mooring line, which inputs the current vessel motions as well as the prior tensions of the mooring line. By only choosing the present vessel motions as input, Sidarta et al. [10] proposed a DNN model to predict mooring line tensions, and Cotrim et al. [13] designed a DNN-based meta-model framework for the computation of FPSO motion to generic winds, waves, and currents. Furthermore, Qiao et al. [15] developed an LSTM model to calculate mooring line tensions of the FPSO by using the vessel motion as the only input and Wang et al. [16] obtained the total mooring line tensions by the superposition of the predicted low frequency and wave frequency tensions employing an LSTM model.

Neural simulations mainly consist of two parts, *i.e.*, solving a single PDE/ODE using neural networks (named neural solver) and learning solution maps of parametric PDE/ODE (named neural operator). The focus of all the previous work was towards the development of neural solvers, which solve the mapping for a specific system, thereby learning the mapping between vector spaces (*i.e.*, finite-dimensional Euclidean spaces). However, for efficient surrogate models, we require higher levels of abstraction, which means the surrogate model needs to generalize for unseen input signals. Recently, a new line of work has proposed the learning between infinite-dimensional spaces employing continuous nonlinear operators developed with DNNs [17, 18]. Unlike the classical DNNs,

neural operators construct interpretable mappings between functions. The neural operators can learn an entire family of equations and have enhanced generalization ability. In 2019, Lu et al. [17] extended the universal operator approximation theorem [19] to propose the idea of deep neural operators (DeepONet), which can learn nonlinear continuous operators accurately and efficiently from a relatively small dataset due to its small generalization error. Later, the idea of neural operators was extended in the frequency domain by modifying the architecture of DeepONet, and Li et al. [18] proposed the Fourier Neural Operator (FNO) and Tripura and Chakraborty [20] developed the wavelet neural operator (WNO).

This paper aims to leverage these three main classes of neural operators to accurately learn the underlying family of PDEs for computing the responses of a moored semi-submersible platform. The accuracy of the solution obtained for unseen cases employing neural operators is compared against the conventional gated recurrent unit (GRU). In this study, the wave elevation is considered as the input, while the responses, including motions of the platform and top tensions of mooring lines, will be obtained as outputs. The underlying learned operator involves the incompressible Navier-Stokes equation and the equation of motion of the moored floating structure. Since the response solutions with zero and non-zero initial conditions are significantly different, separate neural operators are considered to learn the solution in each of the scenarios. Finally, this study will explore the capability of operators to learn from limited labeled datasets. Additionally, two novel extensions of the neural operators, namely the wavelet-DeepONet (W-DeepONet) and the self-adaptive WNO (SA-WNO), are proposed as these extensions have been shown to produce inferences more accurately than their vanilla counterparts.

The paper is organized as follows. In Section 2, we present the numerical solution for computing the response of a floating structure under incident waves and the data generation process. In Section 3, we describe the architectures of the neural operators along with the existing extensions. Additionally, in this section, we also present the details of W-DeepONet and SA-WNO, which are proposed to increase the prediction accuracy of their vanilla counterparts. In Section 4, we compare the performance of the studied models for the responses of a floating structure. Finally, we summarize our observations and provide concluding remarks in Section 5.

2. Formulation for computing the response of a floating structure

The computation of the response of a floating structure under incident waves is complex since it involves two nonlinear operators (*i.e.*, the hydrodynamic operator and the structural operator). The hydrodynamic operator can be regarded as the incompressible Navier-Stokes equation, which takes as input the wave elevation $\eta(t)$ and outputs the hydrodynamic coefficients (*i.e.*, the added mass and potential damping) and wave forces. The structural operator is defined through the equation of motion of the floating structure, which takes the hydrodynamic coefficients and wave force as input and the structural response is obtained as the output.

In the present work, we try to learn a combined operator that integrates the hydrodynamic and structural operators. To that end, the wave elevation is considered as the input and the structural responses are obtained as outputs. Here, the structural response includes the motion of the floater represented by six degrees of freedom and the top tensions of mooring lines. The combined operator of a moored rigid floating structure under the incident wave can be written as [21]:

$$(\mathbf{M} + \mathbf{A})\ddot{\mathbf{x}}(t) + \int_0^t \mathbf{K}(t - \tau)\dot{\mathbf{x}}(\tau)d\tau + \mathbf{C}\mathbf{x}(t) + \mathbf{f}_{moor}(\mathbf{x}(t), \dot{\mathbf{x}}(t)) = \mathbf{f}_{wa}(\eta(t)), \quad (1)$$

where $\mathbf{M}, \mathbf{A}, \mathbf{C} \in \mathbb{R}^{6 \times 6}$ are the body mass, constant added mass, and the linearized hydrostatic restoring force coefficient, respectively; $\mathbf{K}(t)$ is the retardation function, which relies on the geometry of the floating structure; $\ddot{\mathbf{x}}(t), \dot{\mathbf{x}}(t), \mathbf{x}(t) \in \mathbb{R}^{6 \times 1}$ are the acceleration, velocity, and displacement of the floating structure, respectively. The mooring force $\mathbf{f}_{moor}(\mathbf{x}(t), \dot{\mathbf{x}}(t)) \in \mathbb{R}^{6 \times 1}$ is a nonlinear function, which is related to the motions of the platform. The wave force $\mathbf{f}_{wa}(\eta(t)) \in \mathbb{R}^{6 \times 1}$ acting on the floater is caused by the incident wave elevation $\eta(t)$, which can be calculated by a diffraction analysis [1, 22].

The learned operator, $\mathbb{G}_{\mathbf{x}}$, of the structural response, that is the solution of Eq. 1, can be written as

$$\mathbf{x}(t) = \mathbb{G}_{\mathbf{x}}(t; \mathbf{x}(t_0), \dot{\mathbf{x}}(t_0), \eta(t)), \quad (2)$$

where $x_i \in \mathbf{x}$, $\mathbf{x} \in \mathbb{R}^{6 \times 1}$, and $\mathbf{x}_i(t_0)$ and $\dot{\mathbf{x}}_i(t_0)$ denote the initial displacements and velocities of the six DOFs, $i = \{1, 2, \dots, 6\}$. As we can see from Eq. 2, the DOFs are decoupled and are only related to the wave elevation and the initial motions of the six-degrees-of-freedom. Thus, Eq. 2 can be expanded as:

$$x_i(t) = \mathbb{G}_{x_i}(t; x_1(t_0), \dot{x}_1(t_0), x_2(t_0), \dot{x}_2(t_0), \dots, x_6(t_0), \dot{x}_6(t_0), \eta(t)).$$

The top tensions of the mooring lines have a direct relationship with the motion of the platform, so the operator of the top tension, $\mathbb{G}_{\mathbf{T}}$, has the following form:

$$T_{moor}(t) = \mathbb{G}_{\mathbf{T}}(t; \mathbf{x}(t_0), \eta(t)). \quad (3)$$

When the initial conditions are kept constant, Eqs. 2 and 3 can be simplified as:

$$\mathbf{x}(t) = \mathbb{G}_{\mathbf{x}}(t; \eta(t)), \quad (4a)$$

$$T_{moor}(t) = \mathbb{G}_{\mathbf{T}}(t; \eta(t)). \quad (4b)$$

According to Eqs. 2-4, the wave elevations and the corresponding structural responses are needed for learning the above mappings by neural networks. The datasets can be obtained through numerical simulations, physical experiments, or field tests. For numerical simulations, irregular wave elevations are usually generated by the linear superposition technique of linear wave components [23]:

$$\eta(t_j) = \sum_{n=1}^N A_n \cos(\omega_n t_j + \theta_n), \quad j = 0, 1, \dots, N-1, \quad (5)$$

where $A_n = \sqrt{2S(\omega_n)\Delta\omega}$, in which $S(\omega_n)$ is the wave spectrum parameterized by the significant wave height and zero-crossing wave period, and θ_n are randomly generated phase angles uniformly distributed between 0 and 2π . The corresponding structural responses are obtained by solving Eq. 1 with numerical methods. Given the complexity of solving Eq. 1, some numerical software, such as Orcaflex, Sesam, and ANSYS, have been developed and widely utilized to compute structural responses. The time length studied for each sample is 200s with a time interval, $\Delta t = 0.2$ s, hence the total number of temporal points $n_t = 1000$. For generating labeled data to learn the operators in Eqs. 4a and 4b with zero initial condition, Eq. 1 is solved using the numerical solvers. However, for learning the operators in Eqs. 2 and 3 with different initial conditions, we first use the solver to obtain the structural responses with zero initial conditions. Then, the wave elevations and the corresponding responses truncated from non-zero time instants (e.g., 400 seconds) are used as the training datasets. For example, we truncate wave elevations and corresponding responses from 400s–600s (total temporal points = 1000), which are used as training/testing data.

In the next section, we elaborate on the architectures of the neural operators, the deep operator network (DeepONet), the Fourier Neural Operator (FNO), and the Wavelet Neural Operator (WNO).

Additionally, we also introduce useful extensions of these operators.

3. Neural Operators

Neural operators learn nonlinear mappings between infinite dimensional functional spaces and provide a unique simulation framework for predicting complex dynamics [4]. Once the neural operators are trained, they can generalize for unseen cases, which means the same network parameters are shared across different input functions. We have implemented three operator networks that have shown promising results so far, the DeepONet [17], the Fourier neural operator (FNO) [18], and the Wavelet neural operator (WNO) [20]. Although the original DeepONet architecture proposed in [17] has shown remarkable success, several extensions have been proposed in [24–26] to modify its implementation and produce efficient and robust architectures. The architectures of DeepONet, FNO, and WNO are shown in Fig. 1.

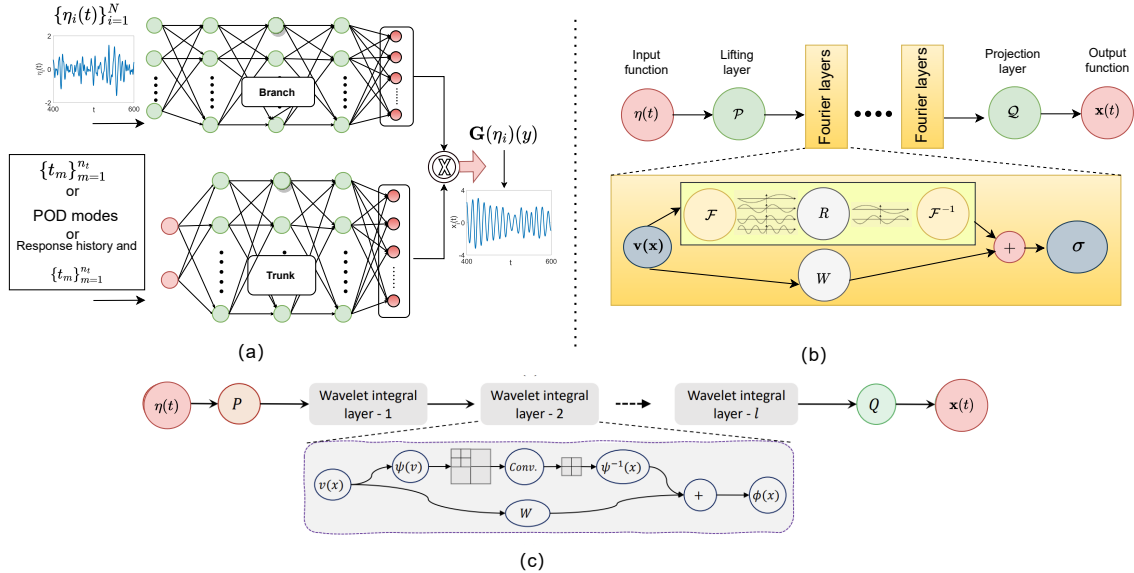


Fig. 1: Architectures of the three neural operators: (a) Deep operator network. If the input to the trunk net is temporal co-ordinates, $\{t_m\}_{m=1}^{n_t}$, it is vanilla DeepONet; if the POD modes are considered in the trunk net, then it is POD-DeepONet; and when the inputs to the trunk net are the historical states along with temporal co-ordinates, it is DeepONet with history), (b) Fourier neural operator, and (c) Wavelet neural operator. For scenarios with zero initial conditions, the branch net of vanilla DeepONet takes as input the wave elevations, and for varying initial conditions, we introduce a second branch network to input the additional initial conditions. In the Fourier and the Wavelet neural operators, the input to the network are wave elevations defined on an equally spaced temporal grid (for zero initial condition). Additionally, for varying initial conditions, the conditions are repeated n_t times to concatenate with the wave elevation and are considered as inputs to the operators.

3.1. Deep Operator Network

The Deep Operator Network (DeepONet) is inspired by the universal approximation theorem for operators [19]. The architecture of DeepONet consists of two DNNs: the branch net encodes the input function, $\eta(t)$, at fixed sensor points, while the trunk net encodes the information related to the temporal coordinates, t_i , at which the solution operator is evaluated to compute the loss function, where $i = \{1, 2, \dots, 1000\}$. To understand the underlying mathematical foundation of DNNs, we consider a network with L hidden layers, where the 0-th layer denotes the input layer and the $(L+1)$ -th layer is the output layer; the weighted input z_i^l into a i^{th} neuron on layer l is a function of weight

\mathbf{W}_{ij}^l and bias \mathbf{b}_j^{l-1} and is represented as:

$$\mathbf{z}_i^l = \mathcal{R}_{l-1} \left(\sum_{j=1}^{m_{l-1}} (\mathbf{W}_{ij}^l(\mathbf{z}_j^{l-1}) + \mathbf{b}_j^l) \right), \quad (6)$$

where $\mathcal{R}_{l-1}(\cdot)$ denotes the activation function of layer l , and m_{l-1} is the number of neurons in layer $l-1$. Based on the above concepts, the feed-forward algorithm for computing the output \mathbf{Y}^L is expressed as follows:

$$\begin{aligned} \mathbf{Y}^L &= \mathcal{R}_L(\mathbf{W}^{L+1}\mathbf{z}^L + \mathbf{b}^L) \\ \mathbf{z}^L &= \mathcal{R}_{L-1}(\mathbf{W}^L\mathbf{z}^{L-1} + \mathbf{b}^L) \\ \mathbf{z}^{L-1} &= \mathcal{R}_{L-2}(\mathbf{W}^{L-1}\mathbf{z}^{L-2} + \mathbf{b}^{L-1}) \\ &\vdots \\ \mathbf{z}^1 &= \mathcal{R}_0(\mathbf{W}^1\mathbf{x} + \mathbf{b}^1), \end{aligned} \quad (7)$$

where \mathbf{x} is the input of the neural network. Eq. 7 can be encoded in compressed form as $\mathbf{Y} = \mathbb{N}(\mathbf{x}; \boldsymbol{\theta})$, where $\boldsymbol{\theta} = (\mathbf{W}, \mathbf{b})$ includes both the weights and biases of the neural network \mathbb{N} .

The branch network takes as input the functions to denote the input realizations $\boldsymbol{\eta} = \{\boldsymbol{\eta}_1, \boldsymbol{\eta}_2, \dots, \boldsymbol{\eta}_N\}$ for N samples, discretized at n_{sen} sensor locations such that $\boldsymbol{\eta}_i = \{\eta_i(t_1), \eta_i(t_2), \dots, \eta_i(t_{n_{sen}})\}$ and $i \in [1, N]$. For a time series problem, as in this case, $n_{sen} = n_t$. The trunk net inputs the temporal locations $\mathbf{y} = \{t_1, t_2, \dots, t_{n_t}\}$ to evaluate the solution operator. Let us assume that the branch network consists of l_{br} hidden layers, where the $(l_{br} + 1)^{\text{th}}$ layer is the output layer consisting of q neurons. Considering an input function $\boldsymbol{\eta}_i$ in the branch network, the network returns a feature embedded in $[b_1, b_2, \dots, b_q]^T$ as output. The output $\mathbf{z}_{br}^{l_{br}+1}$ of the feed-forward branch neural network is expressed as:

$$\begin{aligned} \mathbf{z}_{br}^{l_{br}+1} &= [br_1, br_2, \dots, br_q]^T \\ &= \mathcal{R}_{br}(\mathbf{W}^{l_{br}}\mathbf{z}^{l_{br}} + \mathbf{b}^{l_{br}+1}), \end{aligned} \quad (8)$$

where $\mathcal{R}_{br}(\cdot)$ denotes the nonlinear activation function for the branch net and

$$\mathbf{z}^{l_{br}} = f_{br}(\eta_i(t_1), \eta_i(t_2), \dots, \eta_i(t_{n_{sen}})),$$

where $f_{br}(\cdot)$ denotes a branch net function. Similarly, consider a trunk network with l_{tr} hidden layers, where the $(l_{tr} + 1)$ -th layer is the output layer consisting of q neurons. The trunk net outputs a feature embedding $[tr_1, tr_2, \dots, tr_q]^T$. The output of the trunk network can be represented as:

$$\begin{aligned} \mathbf{z}_{tr}^{l_{tr}+1} &= [tr_1, tr_2, \dots, tr_q]^T \\ &= \mathcal{R}_{tr}(\mathbf{W}^{l_{tr}}\mathbf{z}^{l_{tr}} + \mathbf{b}^{l_{tr}+1}), \end{aligned} \quad (9)$$

where $\mathcal{R}_{tr}(\cdot)$ denotes the nonlinear activation function for the trunk net and $\mathbf{z}^{l_{tr}-1} = f_{tr}(t_1, t_2, \dots, t_{n_t})$. The key point is that we uncover a new operator $\mathbb{G}_{\boldsymbol{\theta}}$ (which is a generalized representation of $\mathbb{G}_{\mathbf{x}}$ and $\mathbb{G}_{\mathbf{T}}$) as a neural network that can infer quantities of interest from unseen and noisy inputs. The two networks are trained to learn the solution operator such that

$$\mathbb{G}_{\boldsymbol{\theta}} : \boldsymbol{\eta}_i \rightarrow \mathbb{G}_{\boldsymbol{\theta}}(\boldsymbol{\eta}_i), \quad \forall i = \{1, 2, 3, \dots, N\}. \quad (10)$$

For a single input function $\boldsymbol{\eta}_i$, the DeepONet prediction $\mathbb{G}_{\boldsymbol{\theta}}(\boldsymbol{\eta})$ evaluated at any coordinate \mathbf{y} can be

expressed as:

$$\begin{aligned}\mathbb{G}_{\theta}(\boldsymbol{\eta}_i)(\mathbf{y}) &= \sum_{k=1}^q \left(\mathcal{R}_{br}(\mathbf{W}_k^{l_{br}} \mathbf{z}_k^{l_{br}-1} + \mathbf{b}_k^{l_{br}}) \cdot \mathcal{R}_{tr}(\mathbf{W}_k^{l_{tr}} \mathbf{z}_k^{l_{tr}-1} + \mathbf{b}_k^{l_{tr}}) \right) \\ &= \sum_{k=1}^q b_k(\eta_i(t_1), \eta_i(t_2), \dots, \eta_i(t_{n_t})) \cdot t_k(\mathbf{y}).\end{aligned}\tag{11}$$

DeepONet requires large annotated datasets of paired input-output observations, but it provides a simple and intuitive model architecture that is fast to train, allowing a continuous representation of the target output functions that is resolution-independent. Conventionally, the trainable parameters of the DeepONet represented by θ in Eq. 11 are obtained by minimizing a loss function. Common loss functions used in the literature include the L_1 - and L_2 -loss functions, defined as:

$$\begin{aligned}\mathcal{L}_1 &= \sum_{i=1}^n \sum_{j=1}^p |\mathbb{G}(\boldsymbol{\eta}_i)(\mathbf{y}_j) - \mathbb{G}_{\theta}(\boldsymbol{\eta}_i)(\mathbf{y}_j)| \\ \mathcal{L}_2 &= \sum_{i=1}^n \sum_{j=1}^p (\mathbb{G}(\boldsymbol{\eta}_i)(\mathbf{y}_j) - \mathbb{G}_{\theta}(\boldsymbol{\eta}_i)(\mathbf{y}_j))^2,\end{aligned}\tag{12}$$

where $\mathbb{G}_{\theta}(\boldsymbol{\eta}_i)(\mathbf{y}_j)$ is the predicted value obtained from the DeepONet, and $\mathbb{G}(\boldsymbol{\eta}_i)(\mathbf{y}_j)$ is the target value. In all the experiments carried out in this work, we have considered a feed-forward fully connected neural network for the branch and the trunk networks.

POD-DeepONet

This is an extension of the standard DeepONet discussed above and was proposed in [24]. The standard DeepONet employs the trunk net to learn the basis of the output function from the data. In this approach, the basis functions are pre-computed by performing proper orthogonal decomposition (POD) on the labelled output of the training data (after the mean has been excluded). The labelled outputs are denoted by $\mathbb{G}(\boldsymbol{\eta}_i)(\mathbf{y})$, where \mathbf{y} denotes the coordinates at which the outputs are computed. The POD basis is used in the trunk net. A DNN is employed in the branch net to learn the POD basis coefficients such that the output can be written as:

$$\mathbb{G}_{\theta}(\boldsymbol{\eta}_i)(\mathbf{y}) = \sum_{k=1}^q br_k(\eta) \phi_k(t) + \phi_0(t),\tag{13}$$

where $\phi_0(t)$ is the mean function of all $\boldsymbol{\eta}_i(\mathbf{y})$, $k = 1, \dots, q$ computed from the training dataset, and $\{\phi_1, \phi_2, \dots, \phi_q\}$ are the q precomputed POD modes of $\mathbb{G}(\boldsymbol{\eta}_i)(\mathbf{y})$.

DeepONet with historical information

This is a modified architecture of DeepONet with additional features of the solution in the trunk network. The trunk network takes as input the n_h historical states of the time signal as the features along with the time step [27, 28]. The input to the branch network remains the same as discussed earlier. We note that in the prediction stage, only the initial data of $\eta(t)$ with the first n_h history terms are given. The predictions from the network itself are concatenated and fed into the trunk net along with the timestep for future predictions.

Self adaptive DeepONet

During the optimization process, some query points must be penalized more than others in order to satisfy constraints (initial condition, boundary condition). In such cases, properly designed non-

uniform training point weights can improve accuracy. These penalizing parameters can be manually modulated but are often a tedious procedure or should be decided adaptively during the training of the DeepONet [29, 30]. These parameters in the loss function can be updated by gradient descent side-by-side with the network parameters. The modified loss function is defined as:

$$\mathcal{L}(\boldsymbol{\theta}, \boldsymbol{\lambda}) = \frac{1}{N} \sum_{i=1}^N g(\boldsymbol{\lambda}) |u_i(\xi) - \mathcal{G}_{\boldsymbol{\theta}}(\mathbf{v}_i)(\xi)|^2, \quad (14)$$

where $g(\lambda)$ is non-negative, strictly increasing self-adaptive mask function, and $\boldsymbol{\lambda} = \{\lambda_1, \lambda_2, \dots, \lambda_j\}$ are j self-adaptive parameters, each associated with an evaluation point, ξ_j . In this work, $j = n_t$. These parameters are constrained to increase monotonically and are always positive. Typically, in a neural network, we minimize the loss function with respect to the network parameters, $\boldsymbol{\theta}$. However, in this approach, we additionally maximize the loss function with respect to the trainable hyper-parameters using a gradient descent/ascent procedure. The modified objective function is defined as:

$$\min_{\boldsymbol{\theta}} \max_{\boldsymbol{\lambda}} \mathcal{L}(\boldsymbol{\theta}, \boldsymbol{\lambda}). \quad (15)$$

The self-adaptive weights are updated using the gradient descent method, such that

$$\boldsymbol{\lambda}^{k+1} = \boldsymbol{\lambda}^k + \eta_{\boldsymbol{\lambda}} \nabla_{\boldsymbol{\lambda}} \mathcal{L}(\boldsymbol{\theta}, \boldsymbol{\lambda}), \quad (16)$$

where $\eta_{\boldsymbol{\lambda}}$ is the learning rate of the self-adaptive weights and

$$\nabla_{\lambda_i} \mathcal{L} = [g'(\lambda_i)(u_i(\xi) - \mathcal{G}_{\boldsymbol{\theta}}(\mathbf{v}_i)(\xi))^2]^T. \quad (17)$$

Therefore, if $g(\lambda_i) > 0$, $\nabla_{\lambda_i} \mathcal{L}$ would be zero only if the term $(u_i(\xi) - \mathcal{G}_{\boldsymbol{\theta}}(\mathbf{v}_i)(\xi))$ is zero. Implementing self-adaptive weights in [30] has considerably improved the accuracy prediction of discontinuities or non-smooth features in the solution.

Wavelet DeepONet

In this section, we develop an extension of the vanilla DeepONet, namely Wavelet DeepONet (W-DeepONet), which is inspired by the efficiency of approximating wavelet components of a time series. The architecture of W-DeepONet consists of two branch nets and two trunk nets, and the inputs for the branch nets and trunk nets are the corresponding wavelet coefficients of the wave elevation $\boldsymbol{\eta}_i$ and the time coordinates \mathbf{y} . The proposed W-DeepONet involves three steps:

- (1) By performing the discrete wavelet transforms of $\boldsymbol{\eta}_i$, \mathbf{y} and the response $\mathbb{G}(\boldsymbol{\eta}_i)(\mathbf{y})$, we obtain the corresponding approximation wavelet coefficients $\boldsymbol{\eta}_{i,A}$, \mathbf{y}_A , $\mathbb{G}(\boldsymbol{\eta}_{i,A})(\mathbf{y}_A)$, and detail wavelet coefficients $\boldsymbol{\eta}_{i,D}$, \mathbf{y}_D , $\mathbb{G}(\boldsymbol{\eta}_{i,D})(\mathbf{y}_D)$;
- (2) The two branch networks encode $\boldsymbol{\eta}_{i,A}$ and $\boldsymbol{\eta}_{i,D}$, while the trunk nets encode the information related to the coordinates \mathbf{y}_A and \mathbf{y}_D , at which the solution operators are evaluated as follows:

$$\mathbb{G}_{\boldsymbol{\theta}}(\boldsymbol{\eta}_{i,A})(\mathbf{y}_A) = \sum_{k=1}^q b_k(\eta_{i,A}(t_1), \eta_{i,A}(t_2), \dots, \eta_{i,A}(t_{n_{sen}})) \cdot t_k(\mathbf{y}_A). \quad (18)$$

$$\mathbb{G}_{\boldsymbol{\theta}}(\boldsymbol{\eta}_{i,D})(\mathbf{y}_D) = \sum_{k=1}^q b_k(\eta_{i,D}(t_1), \eta_{i,D}(t_2), \dots, \eta_{i,D}(t_{n_{sen}})) \cdot t_k(\mathbf{y}_D). \quad (19)$$

The trainable parameters of the W-DeepONet, represented by $\boldsymbol{\theta}$, in Eqs. 18 and 19 are obtained by

minimizing the following loss function:

$$\mathcal{L}_2 = \sum_{i=1}^n \sum_{j=1}^p (\mathbb{G}(\boldsymbol{\eta}_{i,A})(\mathbf{y}_A) - \mathbb{G}_{\boldsymbol{\theta}}(\boldsymbol{\eta}_{i,A})(\mathbf{y}_A))^2 + \sum_{i=1}^n \sum_{j=1}^p (\mathbb{G}(\boldsymbol{\eta}_{i,D})(\mathbf{y}_D) - \mathbb{G}_{\boldsymbol{\theta}}(\boldsymbol{\eta}_{i,D})(\mathbf{y}_D))^2. \quad (20)$$

(3) After the solution operators $\mathbb{G}_{\boldsymbol{\theta}}(\boldsymbol{\eta}_{i,A})(\mathbf{y}_A)$ and $\mathbb{G}_{\boldsymbol{\theta}}(\boldsymbol{\eta}_{i,D})(\mathbf{y}_D)$ are obtained, the inverse wavelet transform is performed to obtain the predicted responses in the time domain.

3.2. Fourier Neural Operator

The Fourier neural operator (FNO) [18] is based on replacing the kernel integral operator with a convolution operator defined in Fourier space. The operator takes input functions defined on a well-defined, equally spaced lattice grid and outputs the field of interest on the same grid points. The network parameters are defined and learned in the Fourier space rather than in the physical space, *i.e.*, the coefficients of the Fourier series of the output function are learned from the data. FNO can be viewed as a DeepONet with a convolution neural network in the branch net to approximate the input functions and Fourier basis functions in the trunk net. In particular, the network has three components: First, the input function $\eta(t)$ is lifted to a higher dimensional representation $\mathbf{h}(x, 0)$, through a lifting layer, \mathcal{P} , which is often parameterized by a linear transformation or a shallow neural network. Then, the neural network architecture is formulated in an iterative manner: $\mathbf{h}(x, 0) \rightarrow \mathbf{h}(x, 1) \rightarrow \mathbf{h}(x, 2) \rightarrow \dots \rightarrow \mathbf{h}(x, L)$, where $\mathbf{h}(x, j)$, $j = 0, \dots, L$, is a sequence of functions representing the values of the architecture at each layer. Each layer is defined as a nonlinear operator via the action of the sum of Fourier transformations and a bias function:

$$\begin{aligned} \mathbf{h}(x, j+1) &= \mathcal{L}_j^{FNO}[\mathbf{h}(x, j)] \\ &:= \sigma(W_j \mathbf{h}(x, j) + \mathcal{F}^{-1}[R_j \cdot \mathcal{F}[\mathbf{h}(\cdot, j)]](x) + \mathbf{c}_j). \end{aligned} \quad (21)$$

Here, we use σ to denote the activation function. W_j , \mathbf{c}_j , and R_j are trainable parameters for the j -th layer, such that each layer has different parameters (*i.e.*, different kernels, weights, and biases). Lastly, the output $\mathbf{u}(x)$ is obtained by projecting $\mathbf{h}(x, L)$ through a local transformation operator layer, \mathbf{Q} .

3.3. Wavelet Neural Operator

The wavelet neural operator (WNO) proposed in [20] learns the network parameters in the wavelet space that are both frequency and spatial localized, hence can learn the patterns in the images and/or signals more effectively. Specifically, the Fourier integral of FNO is replaced by wavelet integrals for capturing the spatial behavior of a signal or for studying the system under complex boundary conditions. It was shown that WNO can handle domains with both smooth and complex geometries, and it was applied in learning solution operators for a highly nonlinear family of PDEs with discontinuities and abrupt changes in the solution domain and the boundary.

Motivated by the idea of self-adaptive DeepONet (SA-DeepONet), in this work, we have introduced self-adaptive WNO. In principle, the idea of this extension is similar to SA-DeepONet, however, to implement it in practice, we have modified Eqs. 16 and 17 such that:

$$\boldsymbol{\lambda}^{k+1} = \boldsymbol{\lambda}^k - \eta_{\lambda} \nabla_{\boldsymbol{\lambda}} \mathcal{L}(\boldsymbol{\theta}, \boldsymbol{\lambda}), \quad (22)$$

$$\nabla_{\lambda_i} \mathcal{L} = [\mathcal{G}_{\boldsymbol{\theta}}(\mathbf{v}_i)(\xi))^2 - g'(\lambda_i)(u_i(\xi))]^T, \quad (23)$$

respectively.

4. Numerical Results

In this section, we have presented the performance of all the neural operators and their extensions discussed in Section 3 for a semi-submersible platform coupled with its mooring system for zero and non-zero initial conditions. Additionally, we have also compared the results of the neural operators with gated recurrent units (GRU). A schematic representation of the structure is shown in Fig. 2, which is composed of a floating offshore platform anchored by eight mooring lines distributed in four groups. The weight of the platform is 53.4×10^3 tons, the length is 105 m, and the working water depth is 234 m. The four groups of mooring lines are evenly distributed at an angle of 90° . For each group, the angle between two mooring lines is 50° . The properties of the mooring lines are listed in Table 1.

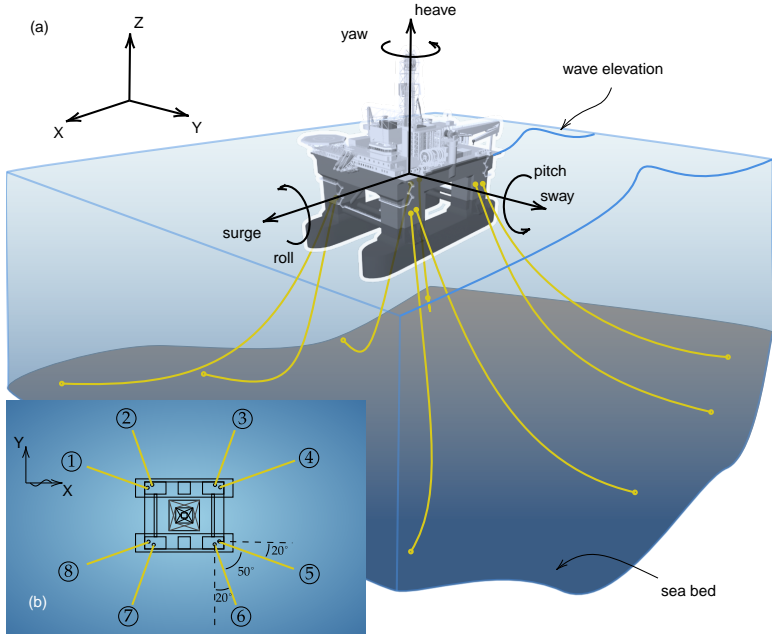


Fig. 2: A schematic representation of a semi-submersible platform with the mooring system: (a) side view, (b) top view

Table 1: Properties of mooring system

Type	Total length (m)	Diameter (mm)	Mass per unit length (kg/m)	Axial stiffness (kN)	Breaking strength (kN)	Added mass coefficient	Inertia coefficient	Drag coefficient
Chain	1700	158.76	154.53	712.7e3	7200	1	0.07	1

The platform is assumed to be subjected to an irregular wave characterized by the JONSWAP spectrum. The realizations of the wave elevations under different sea states are constructed by the superposition technique of linear wave components [23]. The frequency of each wave component is obtained from the discretized JONSWAP spectrum. The heading angle is always considered to be 0° , which implies that only the surge, heave, and pitch of the platform should be investigated. Therefore, only these three degrees of freedom are the focus of the current effort. Due to symmetry and similar characteristics of mooring lines, only the top tension of mooring line #1 is learned. The labeled datasets are generated by running a commercial software *Orcaflex*, which carries out the dynamic coupling analysis of the semi-submersible platform and the mooring systems. We have not considered experimental or field data in the present work. If newly measured environmental and

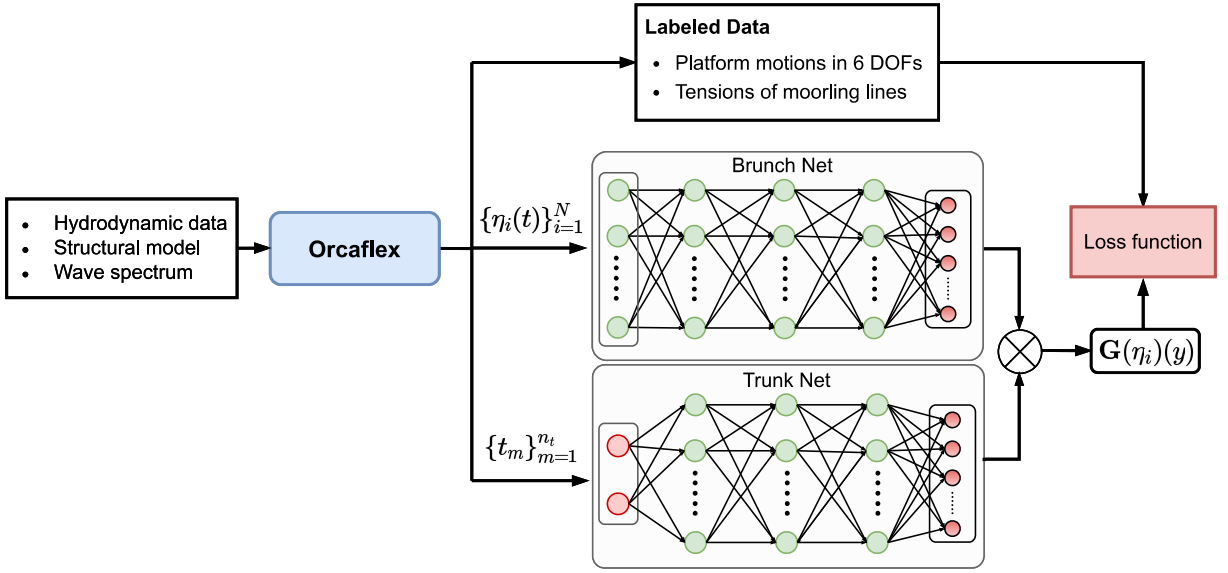


Fig. 3: The workflow of the setup is presented. The discretized JONSWAP spectrum, the hydrodynamic data (e.g., the added mass, potential damping and wave load RAO), and the model of the floating structure is provided as input to the ORCAFLEX, which outputs the wave elevations, $\eta(t)$, the six degrees of freedom (heave, pitch, surge, roll, yaw, and sway), and the tensions of mooring lines on the temporal scale. The outputs of Orcaflex are used to train the neural operators as shown in Fig. 1.

response data from in-service platforms are available, the accuracy of the surrogate model can be continuously improved and updated. DeepONet and its extensions and GRU have been implemented using Tensorflow [31], while FNO and WNO along with their extensions have been implemented using the PyTorch [32]. Moreover, we have employed the Adam optimizer and random norm initialization, unless otherwise mentioned. The experiments carried out in this work are listed in Table 2. Details about the network architecture adopted in each case for every operator are presented in Appendix C. For a visual representation, additional plots of the predictions compared against the ground truth are shown in Appendix A.

For cases 1 and 6, we have considered the sea state with significant wave height, $H_s = 5.5\text{m}$, and zero-crossing wave period, $T_z = 13.5\text{s}$. For cases 2 and 7, we have generated samples for the sea states with combinations of H_s and T_z drawn from the sets: $H_s = [3.5, 4.5]$ and $T_z = [7.5, 8.5, 9.5, 10.5]$, of which the dataset with $H_s = 3.5\text{m}$ and $T_z = 8.5\text{s}$ is considered for validation and testing and the rest is used for training the network. For cases, 3 and 8, the number of samples generated for each combination of H_s and T_z are shown in Table 3. From the generated samples, the data for $H_s = 2.5\text{m}$ and $T_z = 9.5\text{s}$ is considered for testing and validation, while the remaining combinations are used for training the operator networks. The errors of the test cases obtained for each case for all the discussed approaches are shown in Fig. 4. Among all the vanilla forms of the neural operators, FNO demonstrates an overall high accuracy in response prediction for all cases. The low prediction accuracy of surge motions employing DeepONet and WNO may be attributed to its broad-band spectrum feature. This conclusion is consistent with that given by Ye et al. [6], which states that the spectrum bandwidth deteriorates the prediction accuracy of DNNs. To that end, we increased the number of samples generated for all combinations of H_s and T_z for surge motion in cases 4 and 5. As expected, the generalization of the neural operators improves in cases 4 and 5.

Furthermore, we also observe a marked improvement in the accuracy of DeepONet when 5 history terms are recursively updated in the trunk net to improve the computation of the basis function which is obtained as outputs from the trunk net. In Figure 4(a)-(d), we show the error (MSE for heave, pitch, and surge, and relative L_2 for tension) between the studied models and ground truth. We observe that all the operators have similar accuracy for heave, pitch and tension, however, for surge, DeepONet with 5 historical states outperform all other operators. Motivated by the accuracy of DeepONet with historical states, we conducted additional experiments by varying the number of historical terms, n_h in the trunk net. Additionally, in 4(e) we present the improvement in the prediction accuracy with varying n_h for approximating the surge motion of case 3. Error plots of heave, pitch, tension lines, and surge for two representative test samples with zero initial conditions for case 3 are shown in Fig. 5 for the best extension of each operator. Furthermore, we also observe that W-DeepONet and SA-WNO are significantly more accurate than their vanilla counterparts for the surge motion.

Table 2: Description of the datasets considered for the experiments performed. The time length considered is 200s with $\Delta t = 0.2$ s, hence $n_t = 1000$ temporal points per signal. For each experiment, N_{tr} , N_{val} , and N_{te} denote the number of training, validation, and testing samples, respectively.

	Case #	Description
Zero initial conditions	Case 1	<p>Training and testing on same sea state.</p> <p>Heave/Pitch: $N_{tr} = 800$, $N_{val} = 100$, $N_{te} = 100$</p> <p>Tension: $N_{tr} = 2800$, $N_{val} = 100$, $N_{te} = 100$</p> <p>Surge: $N_{tr} = 7200$, $N_{val} = 400$, $N_{te} = 400$</p>
	Case 2	<p>Training on 7 sea states & testing on an unknown sea state.</p> <p>$N_{tr} = 14,000$, $N_{val} = 1,000$, $N_{te} = 1,000$</p>
	Case 3	<p>Training on 72 sea states with limited samples & testing on an unknown sea state.</p> <p>$N_{tr} = 959$, $N_{val} = 23$, $N_{te} = 20$</p>
	Case 4	<p>Training on 72 sea states & testing on an unknown sea state.</p> <p>$N_{tr} = 14,400$, $N_{val} = 100$, $N_{te} = 100$</p>
	Case 5	<p>Training on 72 sea states & testing on an unknown sea state.</p> <p>$N_{tr} = 21,600$, $N_{val} = 100$, $N_{te} = 200$</p>
Varying initial conditions	Case 6	<p>Training and testing on same sea state.</p> <p>Heave/Pitch: $N_{tr} = 800$, $N_{val} = 100$, $N_{te} = 100$</p> <p>Tension: $N_{tr} = 2800$, $N_{val} = 100$, $N_{te} = 100$</p> <p>Surge: $N_{tr} = 7200$, $N_{val} = 400$, $N_{te} = 400$</p>
	Case 7	<p>Training on 7 sea states & testing on an unknown sea state.</p> <p>$N_{tr} = 14,000$, $N_{val} = 1,000$, $N_{te} = 1,000$</p>
	Case 8	<p>Training on 72 sea states with limited samples & testing on an unknown sea state.</p> <p>$N_{tr} = 959$, $N_{val} = 23$, $N_{te} = 20$</p>
	Case 9	<p>Training on 72 sea states & testing on an unknown sea state.</p> <p>$N_{tr} = 14,400$, $N_{val} = 100$, $N_{te} = 100$</p>
	Case 10	<p>Training on 72 sea states & testing on an unknown sea state.</p> <p>$N_{tr} = 21,600$, $N_{val} = 100$, $N_{te} = 200$</p>

Table 3: The sea states described in Table 2 are defined by their wave height (H_s) and zero crossing wave period (T_z). For cases 1 and 6, the blue-marked case is considered, while the green-marked zone is used for cases 2 and 7. The table includes all relevant sea states for cases 3-5 and 8-10. In cases 3 and 8, which test the model's performance with sparse data, the number of samples generated for each sea state is equal to the value of the cell at the intersection of the components, H_s and T_z . These sea states are specific to the North Atlantic Ocean.

H_s (m)	T_z (s)										Total
	4.5	5.5	6.5	7.5	8.5	9.5	10.5	11.5	12.5	13.5	
0.5	3	14	21	13	4	1					56
1.5		13	54	75	47	16	4	1			210
2.5		5	33	79	80	43	14	4	1		259
3.5		1	14	46	65	48	21	6	2		203
4.5			5	21	38	34	19	7	2		126
5.5			2	9	19	20	13	5	2	1	71
6.5			1	3	8	11	8	4	2	1	38
7.5				1	4	5	4	2	1		17
8.5				1	2	3	3	2	1		12
9.5					1	1	2	1	1		6
10.5						1	1	1			3
11.5							1				1
Total	3	33	130	248	268	183	90	33	12	2	1002

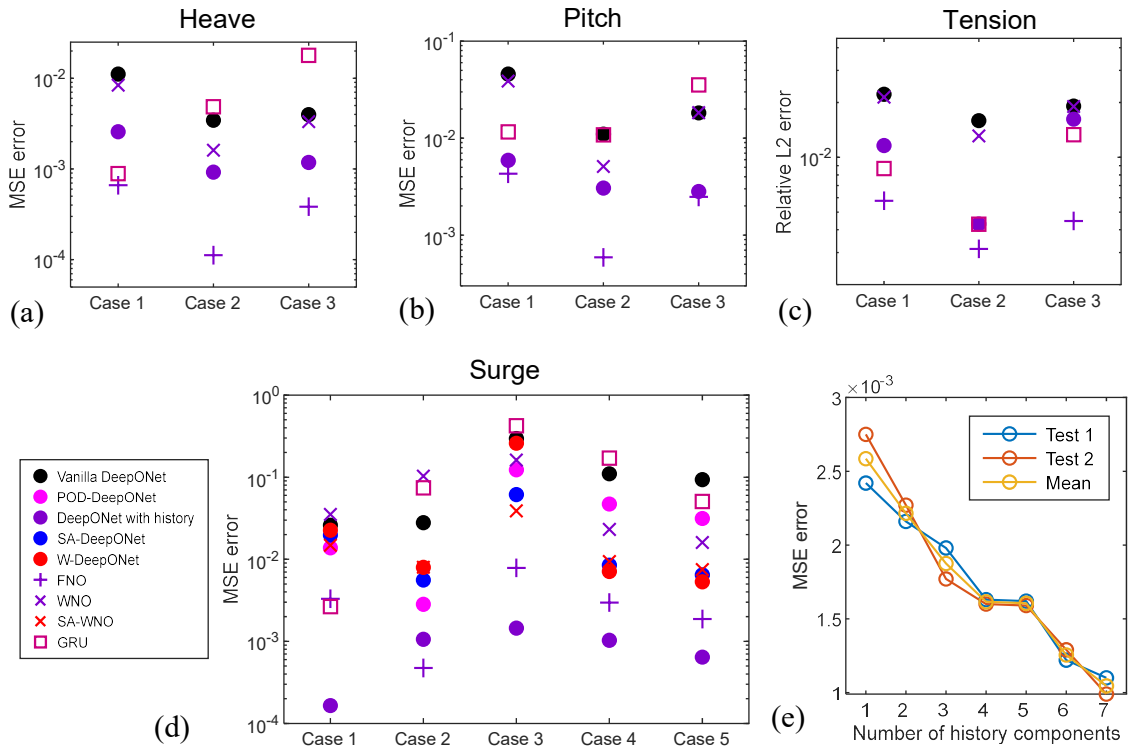


Fig. 4: Error in the test cases for (a) heave and (b) pitch motions, (c) tension lines, and (d) surge motion for all the neural operators and their extensions for cases 1–5, that considers zero initial conditions. (e) Influence of the number of history terms, n_h in the test accuracy for case 5 to approximate the surge motion with history DeepONet that employs historical states as basis enhancements along with the temporal coordinates in the trunk net. In all the plots, $n_h = 5$.

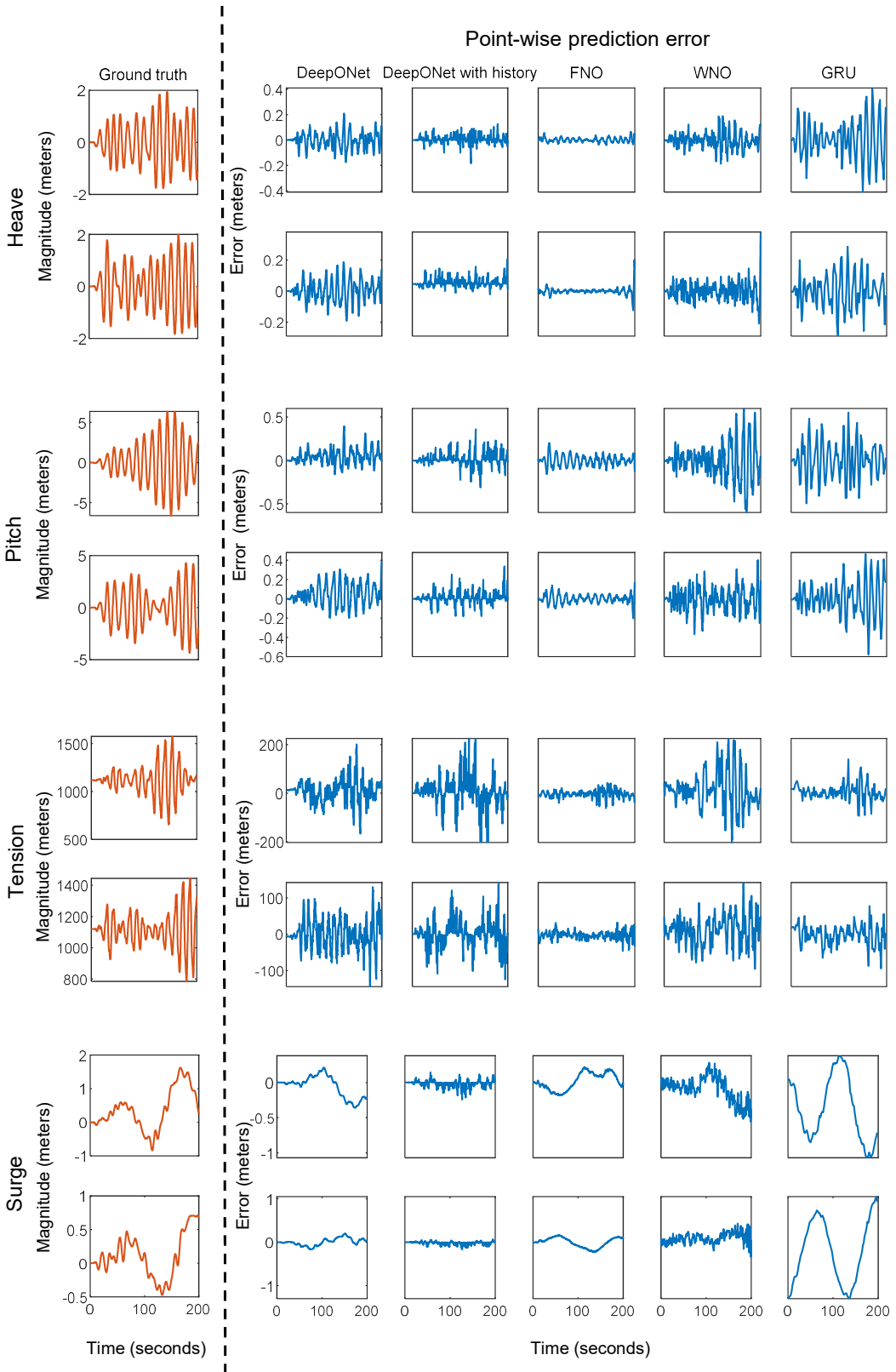


Fig. 5: Pointwise error plots of heave and pitch motions, tension lines, and surge motion for two representative test samples drawn from case 3 that considers zero initial conditions. The ground truth is shown in the left column and the pointwise error for vanilla-DeepONet, DeepONet with 5 historical states, FNO, vanilla WNO, and GRU are presented in the right section.

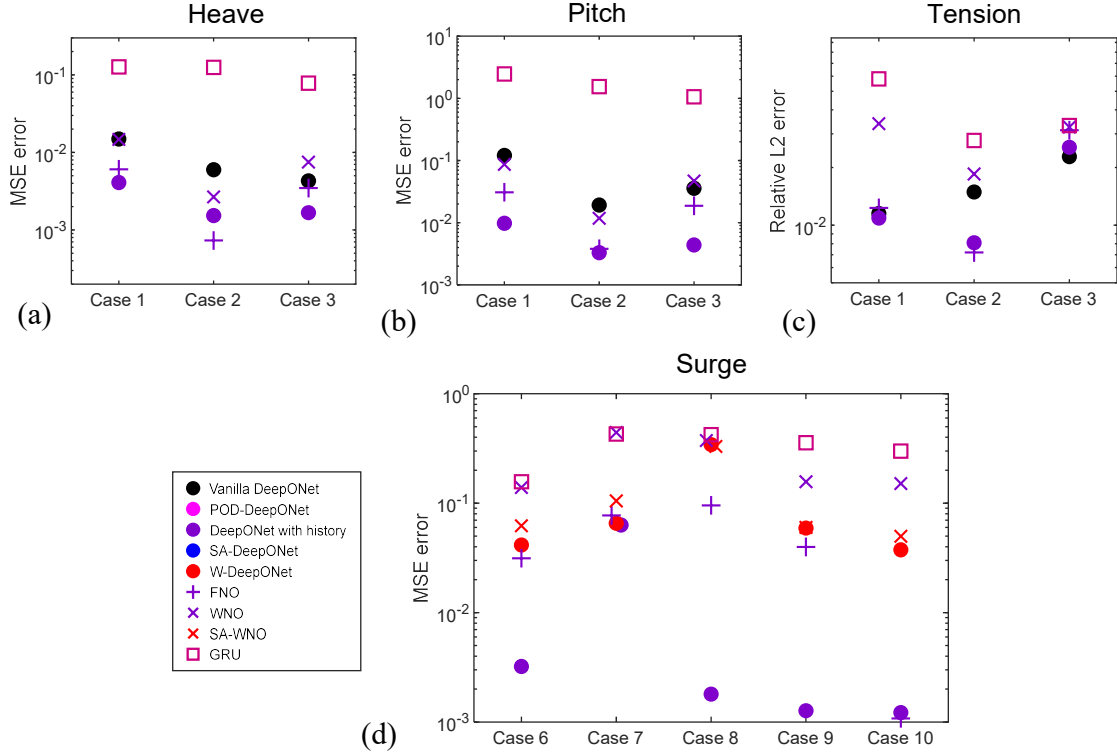


Fig. 6: Error in the test cases for (a) heave and (b) pitch motions, (c) tension lines, and (d) surge motion for all the neural operators and their extensions for cases 6–10, that considers 6 varying initial conditions. In (d), $n_h = 5$ historical terms have been considered for approximating the surge.

When a semi-submersible platform floats in the sea, a very likely situation is that the floater is not static. This situation will lead to non-zero initial conditions. On the other hand, if an ergodic signal is divided into multiple samples to learn the response, the initial conditions for these samples are also different. Thus, it is meaningful to establish a model to learn the operator which maps the wave elevation $\eta(t)$ and initial conditions $(\mathbf{x}(t_0), \dot{\mathbf{x}}(t_0))$ to the structural response $\mathbf{x}(t)$, as shown in Eqs. 2 and 3. The experiments carried out for zero initial conditions of the responses (cases 1–5) are repeated with different initial conditions (cases 6–10). The architecture of the operators is modified such that:

- 1) DeepONet and its extensions have an additional branch network to input the initial condition. The additional branch net inputs the value of 6 initial conditions (3 for displacement and 3 for velocity), therefore $n_{sen} = 6$ for the added branch network.
- 2) FNO, WNO, and its extensions consider the initial conditions as 6 additional input functions (3 for displacement and 3 for velocity). To that end, the initial conditions are repeated n_t times, as the input functions have to be defined for every grid point.

The errors obtained in N_{te} test cases for all approaches for cases 6–10 are shown in Fig. 6. We observe that all the neural operators are significantly more accurate than GRU. Considering the heave and pitch motion and tension lines, the vanilla neural operators have similar accuracy in the prediction of unseen test cases. However, for the surge motion, DeepONet with 5 historical states and the time in the trunk net outperforms all the other operators and their extensions. We also observe a significant deterioration in the generalization accuracy of FNO for the surge motion with

different initial conditions compared to the predictions with zero initial conditions (see Fig.4). It can be concluded that FNO does not work well for capturing transient responses. Error plots of heave, pitch, tension lines, and surge for two representative test samples with different initial conditions for case 8 are shown in Fig. 7. Additionally, the error plots for two test samples with W-DeepONet and SA-WNO are shown in Fig. 8

Considering that capturing the surge motion is the most challenging, to evaluate the performance of the model, we compute the mean square error of predictions, and we report the mean and standard deviation of this metric based on three independent training trials in Appendix B.

5. Summary

In this work, we performed an extensive study for evaluating the accuracy and performance of three neural operators, namely the deep operator network (DeepONet), the Fourier neural operator (FNO), and the Wavelet neural operator (WNO) along with their extensions to approximate the three significant degrees of motion out of a total of six degrees for a semi-submersible platform under incident waves. Alongside neural operators, the study also considers the accuracy and performance of Gated recurrent units (GRU), which is a type of recurrent neural network that has been shown to learn long sequences more accurately than traditional neural networks. We have systematically studied the capability of the models for zero and non-zero initial conditions of displacement and velocities of the waves, for scenarios where the model was trained and tested with the data drawn for the same wave height and the time period, and also for situations where the model was tested with an unseen description of the wave height and time period. Additionally, we have proposed two novel extensions of the neural operators, namely the wavelet-DeepONet (W-DeepONet) and the self-adaptive WNO (SA-WNO).

Of all the experiments studied in this work, cases 3 and 8 are the most challenging considering the availability of extremely limited labeled training data spanned over a broad range of wave height and time period. The training of the neural operators is followed by online inference, which could be used for real-time response prediction for any sea state and varying initial conditions of displacement and velocity. Our observations can be summarized as follows:

1. For a small bandwidth of the frequency spectrum (heave, pitch, and top tensions of the platform's mooring line), and non-transient responses, FNO outperforms all the operators and their extensions (see Fig. 4(a)–(c)).
2. Considering transient responses in small bandwidth (different initial conditions for displacement and velocities), the prediction accuracy of FNO is drastically reduced compared to capturing non-transient responses. It is observed that in such scenarios DeepONet with $n_h = 5$ historical terms achieves better accuracy (see Fig.6(a)–(c)).
3. Addition of historical states to the trunk net along with the temporal co-ordinates for obtaining better basis functions results in a drastic improvement in the accuracy for approximating the surge motion with DeepONet (DeepONet with history, see Fig. 4(d) and 6(d)). The accuracy can be further improved by increasing the number of historical states (see Fig. 4(e)).
4. Of all the experiments conducted, GRU approximates the solution with reasonable accuracy only in case 1, where the training and the testing data are drawn from the same sea state for zero initial conditions (Fig. 4(a)–(c)). This indicates that such networks cannot be used for the efficient generalization of solutions across multiple PDEs/ODEs. Additionally, GRUs have deteriorated performance when multiple functions are considered to be approximated at the same time (non-zero initial condition, see Fig.6(a)–(c)).

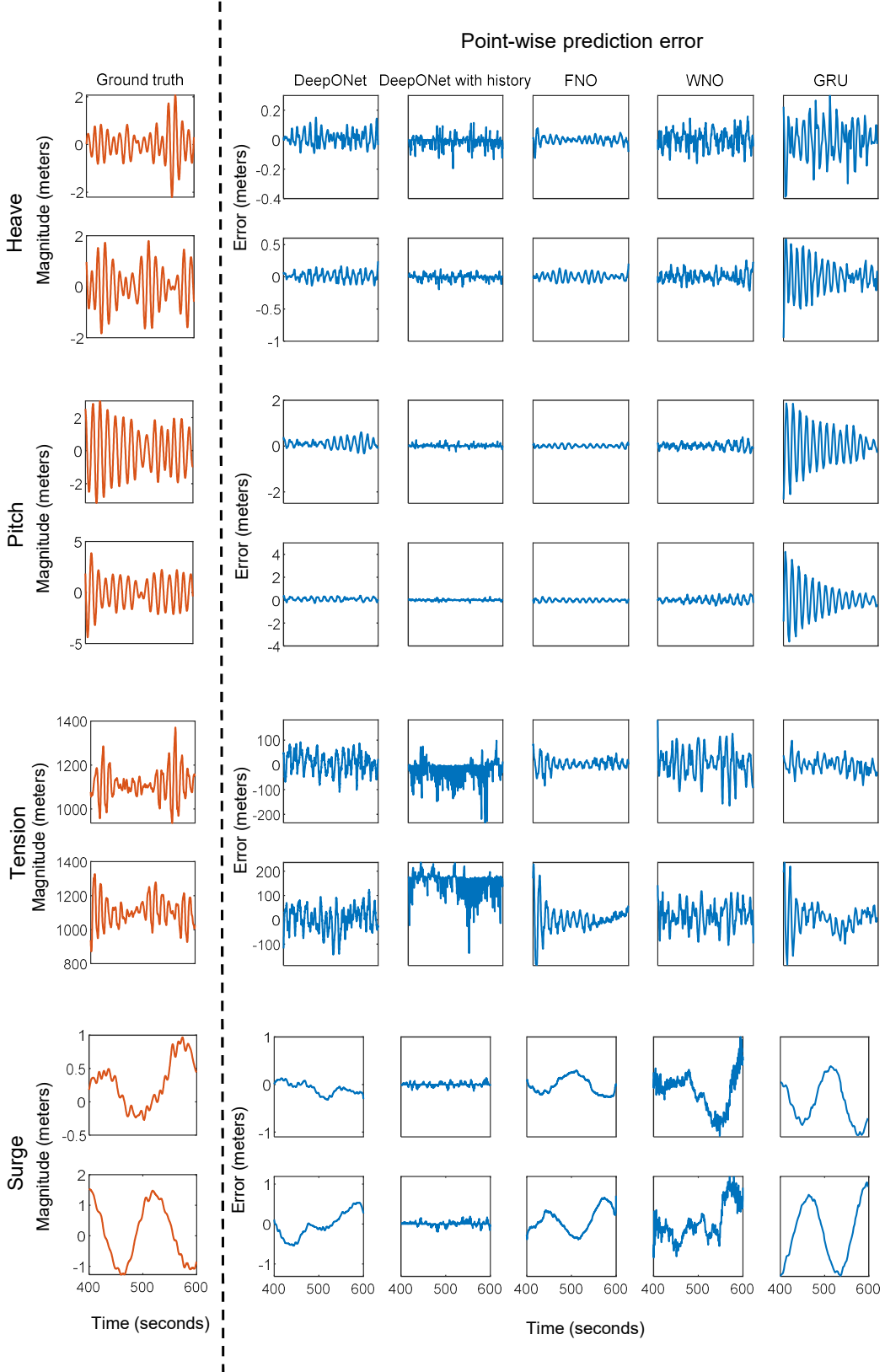


Fig. 7: Pointwise error plots of heave and pitch motions, tension lines, and surge motion for two representative test samples drawn from case 8 that considers varying initial conditions. The ground truth is shown in the left column and the pointwise error for vanilla-DeepONet, DeepONet with 5 historical states, FNO, vanilla WNO, and GRU are presented in the right section.

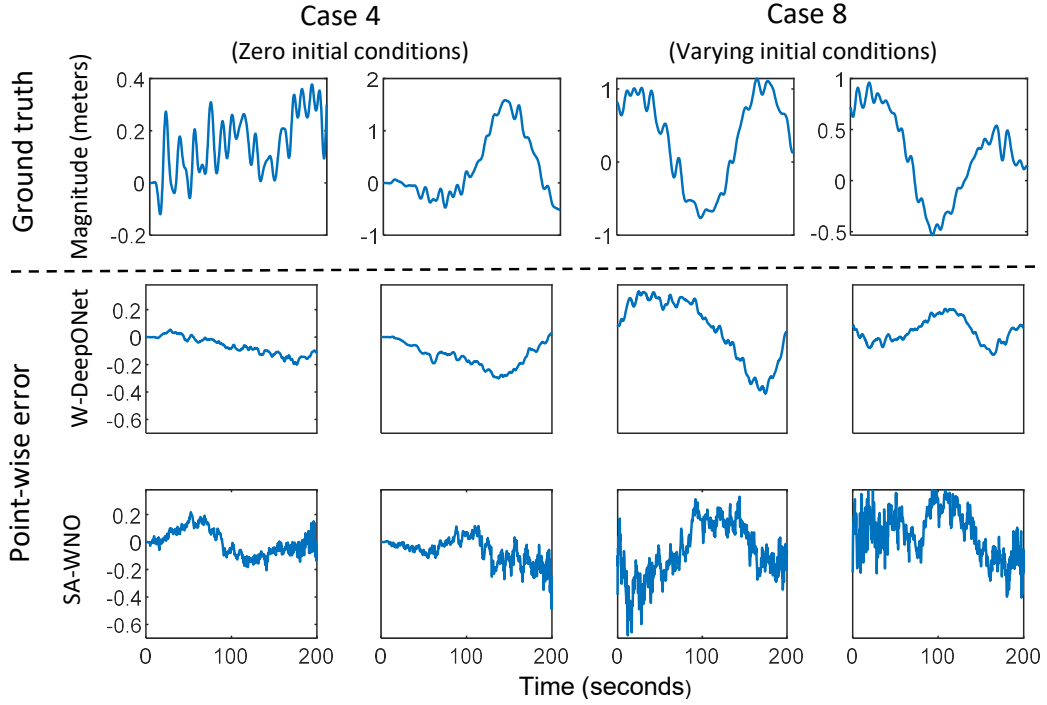


Fig. 8: Point-wise error for representative test samples with W-DeepONet and SA-WNO. The first two columns are for the solution with zero initial conditions and the last two columns are with varying initial conditions.

5. Since the input and output dimensions in FNO and WNO needs to be the same, enhancing the performance by adding historical information cannot be performed.
6. The neural operator extensions proposed through this study (W-DeepONet and SA-WNO) perform considerably well than their vanilla counterparts. The predictive accuracy of W-DeepONet is similar to SA-WNO in capturing both transient and non-transient responses for the surge motion. However, the prediction accuracy of SA-WNO is very sensitive to parameters, especially batch size.
7. The improvement in the predictive accuracy and generalization of test cases with larger training data (case 5 > case 4 > case 3 and case 10 > case 9 > case 8) is established.
8. For 1000 samples, the trained neural operators predicted the outcomes in less than 10 seconds. By using 40 parallel threads, the Orcaflex software finished in roughly a half-hour. The findings demonstrated that a complete dynamic analysis was outperformed by neural operators with high precision in terms of the speed at which structural responses were delivered by more than two orders of magnitude.
9. Additionally, depending on newly measured environmental and response data of in-service platforms, the neural operators based on the numerical data can be partially re-trained and continuously updated.

Acknowledgement

QS would like to acknowledge the scholarship from the Dalian University of Technology for visiting Brown University, U.S.A. SG and GEK would like to acknowledge support by the DOE

project PhILMs (Award Number DE-SC0019453) and the OSD/AFOSR MURI grant FA9550-20-1-0358. The authors would like to acknowledge the computing support provided by the computational resources and services at the Center for Computation and Visualization (CCV), Brown University where all experiments were carried out.

Code availability

The codes for the two operator extensions (W-DeepONet and SA-WNO) developed as a part of this work will be made publicly available on GitHub.

References

- [1] O. Faltinsen, *Sea Loads on Ships and Offshore Structures*, Vol. 1, University Press, 1993.
- [2] M. Diez, A. Serani, E. F. Campana, F. Stern, Time-series forecasting of ships maneuvering in waves via dynamic mode decomposition, *Journal of Ocean Engineering and Marine Energy* 8 (4) (2022) 471–478.
- [3] K. Fukami, T. Murata, K. Zhang, K. Fukagata, Sparse identification of nonlinear dynamics with low-dimensionalized flow representations, *Journal of Fluid Mechanics* 926 (2021) A10.
- [4] S. Goswami, M. Yin, Y. Yu, G. E. Karniadakis, A physics-informed variational DeepONet for predicting crack path in quasi-brittle materials, *Computer Methods in Applied Mechanics and Engineering* 391 (2022) 114587.
- [5] X. Guo, X. Zhang, X. Tian, X. Li, W. Lu, Predicting heave and surge motions of a semi-submersible with neural networks, *Applied Ocean Research* 112 (2021) 102708.
- [6] Y. Ye, L. Wang, Y. Wang, L. Qin, An EMD-LSTM-SVR model for the short-term roll and sway predictions of semi-submersible, *Ocean Engineering* 256 (2022) 111460.
- [7] M. Schirrmann, M. Collette, J. Gose, Data-driven models for vessel motion prediction and the benefits of physics-based information, *Applied Ocean Research* 120 (2022) 102916.
- [8] C. Liong, K. Chua, Data assimilation for deterministic prediction of vessel motion in real-time, *Ocean Engineering* 244 (2022) 110356.
- [9] N. Christiansen, P. E. Torbergsen V, J. Høgsberg, N. Sødahl, Efficient Mooring Line Fatigue Analysis Using a Hybrid Method Time Domain Simulation Scheme, in: *International Conference on Offshore Mechanics and Arctic Engineering*, Vol. 55317, American Society of Mechanical Engineers, 2013, p. V001T01A035.
- [10] D. Sidarta, J. Kyoung, J. Oj-Sullivan, K. Lambrakos, Prediction of Offshore Platform Mooring Line Tensions Using Artificial Neural Network, in: *International Conference on Offshore Mechanics and Arctic Engineering*, Vol. 57632, American Society of Mechanical Engineers, 2017, p. V001T01A079.
- [11] D. Lee, S. Lee, J. Lee, Standardization in building an ANN-based mooring line top tension prediction system, *International Journal of Naval Architecture and Ocean Engineering* 14 (2022) 100421.

- [12] M. Arifuzzaman, M. Uddin, M. Jameel, M. Towhidur Rahman B, Nonlinear Response Prediction of Spar Platform in Deep Water Using an Artificial Neural Network, *Applied Sciences* 12 (12) (2022) 5954.
- [13] L. Cotrim, R. Barreira, I. Santos, E. S. Gomi, A. Costa, E. Tannuri, Neural Network Meta-Models for FPSO Motion Prediction From Environmental Data With Different Platform Loads, *IEEE Access* 10 (2022) 86558–86577.
- [14] D. Kwon, C. Jin, M. Kim, Prediction of dynamic and structural responses of submerged floating tunnel using artificial neural network and minimum sensors, *Ocean Engineering* 244 (2022) 110402.
- [15] D. Qiao, P. Li, G. Ma, X. Qi, J. Yan, D. Ning, B. Li, Realtime prediction of dynamic mooring lines responses with LSTM neural network model, *Ocean Engineering* 219 (2021) 108368.
- [16] Z. Wang, D. Qiao, J. Yan, G. Tang, B. Li, D. Ning, A new approach to predict dynamic mooring tension using LSTM neural network based on responses of floating structure, *Ocean Engineering* 249 (2022) 110905.
- [17] L. Lu, P. Jin, G. Pang, Z. Zhang, G. Karniadakis, Learning nonlinear operators via DeepONet based on the universal approximation theorem of operators, *Nature Machine Intelligence* 3 (3) (2021) 218–229.
- [18] Z. Li, N. Kovachki, K. Azizzadenesheli, B. Liu, K. Bhattacharya, A. Stuart, A. Anandkumar, Fourier Neural Operator for Parametric Partial Differential Equations, *arXiv preprint arXiv:2010.08895* (2020).
- [19] T. Chen, H. Chen, Universal approximation to nonlinear operators by neural networks with arbitrary activation functions and its application to dynamical systems, *IEEE Transactions on Neural Networks* 6 (4) (1995) 911–917.
- [20] T. Tripura, S. Chakraborty, Wavelet Neural Operator for solving parametric partial differential equations in computational mechanics problems, *Computer Methods in Applied Mechanics and Engineering* 404 (2023) 115783.
- [21] W. Cummins, W. Iiuhl, A. Uinm, The Impulse Response Function and Ship Motions, *Schiffstechnik* (1962).
- [22] J. Pinkster, Mean and low frequency wave drifting forces on floating structures, *Ocean Engineering* 6 (6) (1979) 593–615.
- [23] S. Hu, Q. Cao, H. Li, Laplace Domain Approach for Computing Transient Response of Simple Oscillators to Stationary Excitation, *Journal of Engineering Mechanics* 144 (9) (2018) 04018093.
- [24] L. Lu, X. Meng, S. Cai, Z. Mao, S. Goswami, Z. Zhang, G. Karniadakis, A comprehensive and fair comparison of two neural operators (with practical extensions) based on FAIR data, *Computer Methods in Applied Mechanics and Engineering* 393 (2022) 114778.

[25] S. Goswami, D. S. Li, B. V. Rego, M. Latorre, J. D. Humphrey, G. E. Karniadakis, Neural operator learning of heterogeneous mechanobiological insults contributing to aortic aneurysms, *Journal of the Royal Society Interface* 19 (193) (2022) 20220410.

[26] S. Goswami, K. Kontolati, M. D. Shields, G. E. Karniadakis, Deep transfer operator learning for partial differential equations under conditional shift, *Nature Machine Intelligence* (2022) 1–10.

[27] V. Oommen, K. Shukla, S. Goswami, R. Dingreville, G. E. Karniadakis, Learning two-phase microstructure evolution using neural operators and autoencoder architectures, *npj Computational Materials* 8 (1) (2022) 190.

[28] L. Liu, K. Nath, W. Cai, A Causality-DeepONet for Causal Responses of Linear Dynamical Systems, *arXiv preprint arXiv:2209.08397* (2022).

[29] L. McClenny, U. Braga-Neto, Self-Adaptive Physics-Informed Neural Networks using a Soft Attention Mechanism, *arXiv preprint arXiv:2009.04544* (2020).

[30] K. Kontolati, S. Goswami, M. D. Shields, G. E. Karniadakis, On the influence of over-parameterization in manifold based surrogates and deep neural operators, *arXiv preprint arXiv:2203.05071* (2022).

[31] A. Agarwal, P. Barham, E. Brevdo, Z. Chen, C. Citro, Tensorflow: A system for large-scale machine learning, in: *Proceedings of the 12th USENIX Conference on Operating Systems Design and Implementation*, USENIX Association, 2016.

[32] A. Paszke, S. Gross, F. Massa, A. Lerer, J. Bradbury, G. Chanan, T. Killeen, Z. Lin, N. Gimelshein, L. Antiga, et al., PyTorch: An Imperative Style, High-Performance Deep Learning Library, *Advances in neural information processing systems* 32 (2019).

Appendix A. Representative plots to show the response obtained from the neural operators.

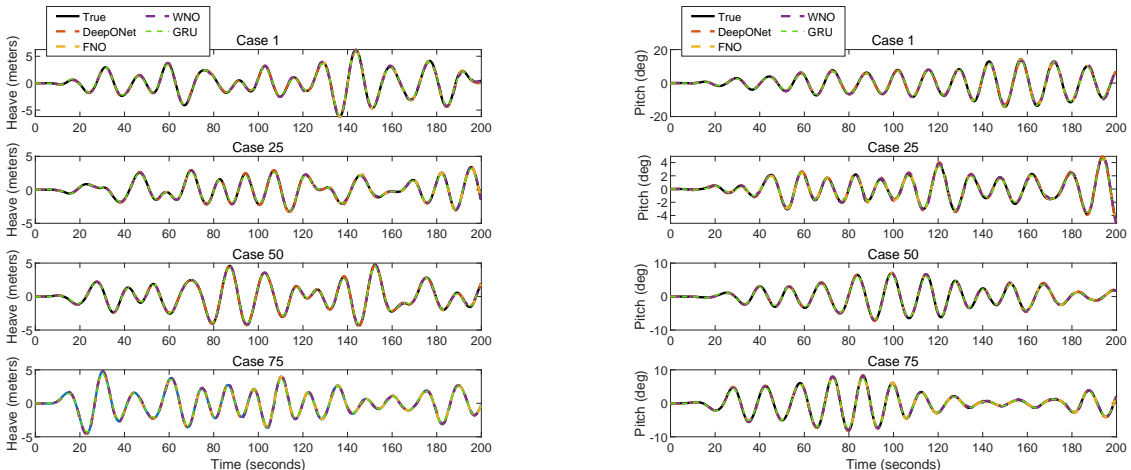


Fig. A.9: Comparison of heave and pitch responses predicted by the four models, DeepONet, FNO, WNO, and GRU against the ground truth in Case 1. The plots on the left show the heave motion, while the plots on the right show the pitch motion.

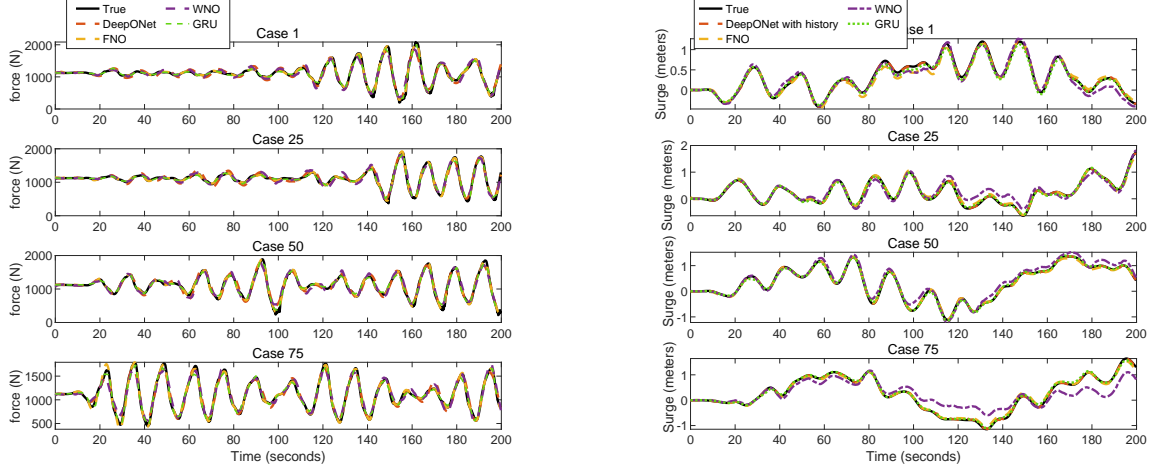


Fig. A.10: Comparison of the top tension of mooring #1 and surge response predictions obtained by the four models against the ground truth in Case 1. The plots on the left show the top tension, while the plots on right show the surge motion.

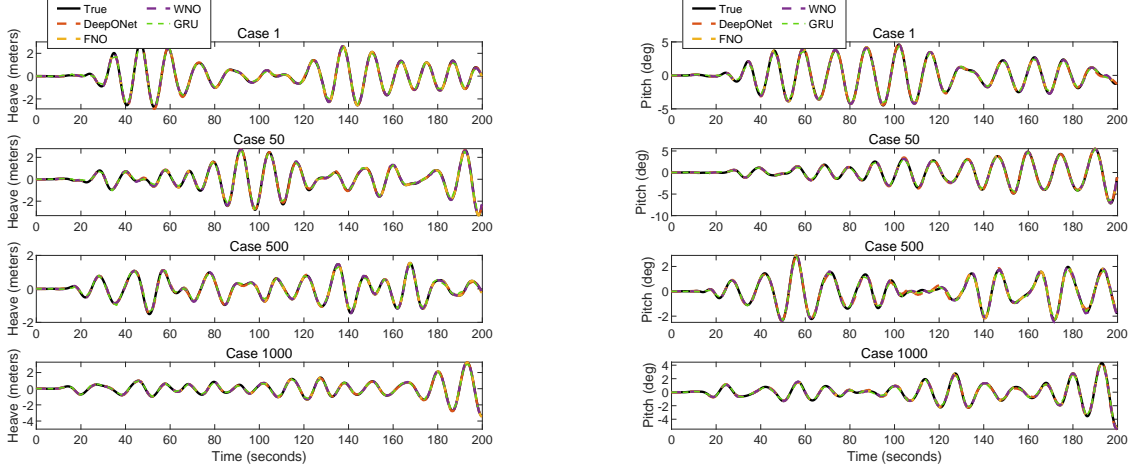


Fig. A.11: Comparison of heave and pitch responses predicted by the four models, DeepONet, FNO, WNO and GRU against the ground truth in Case 2. The plots on left show the heave motion, while the plots on right show the pitch motion.

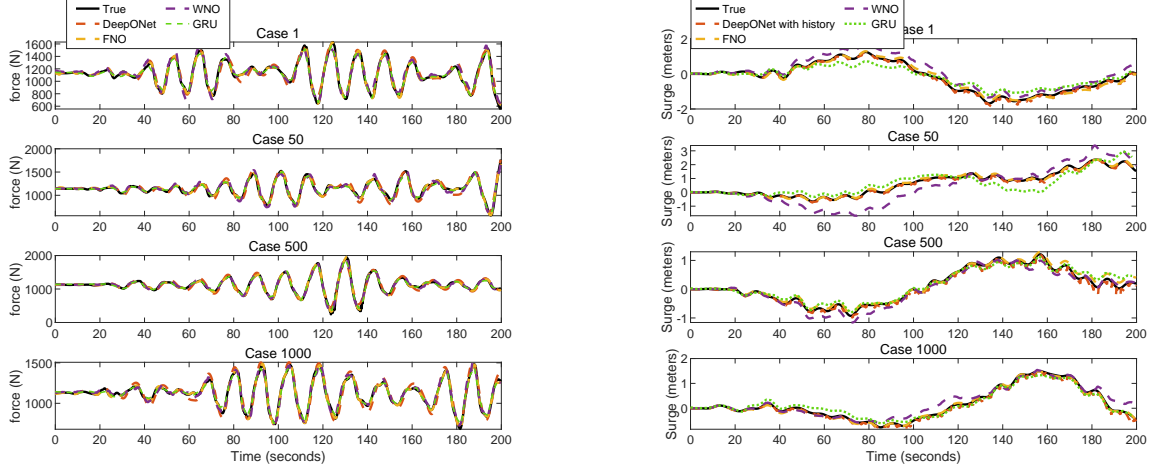


Fig. A.12: Comparison of the top tension of mooring #1 and surge response predictions obtained by the four models against the ground truth in Case 2. The plots on left show the top tension, while the plots on right show the surge motion.

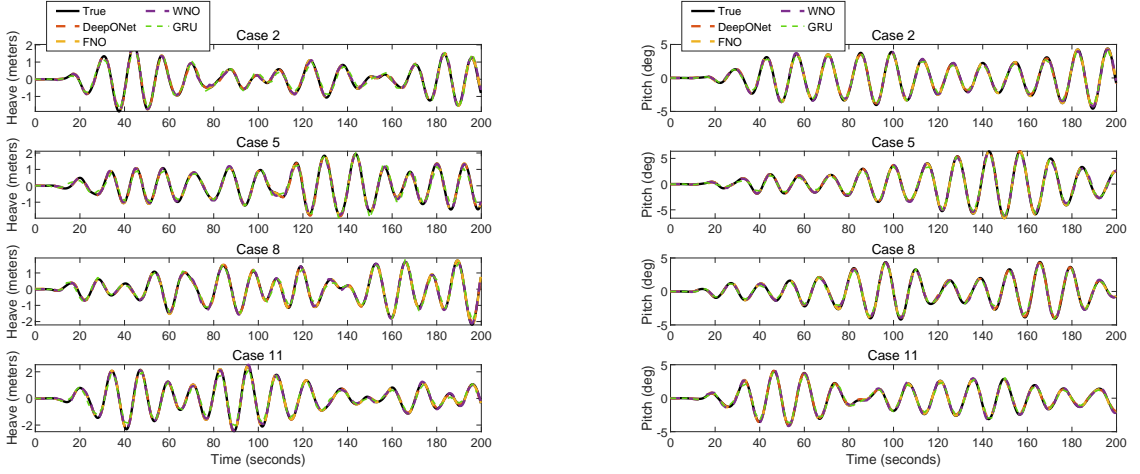


Fig. A.13: Comparison of heave and pitch responses predicted by the four models, DeepONet, FNO, WNO and GRU against the ground truth in Case 3. The plots on left show the heave motion, while the plots on right show the pitch motion.

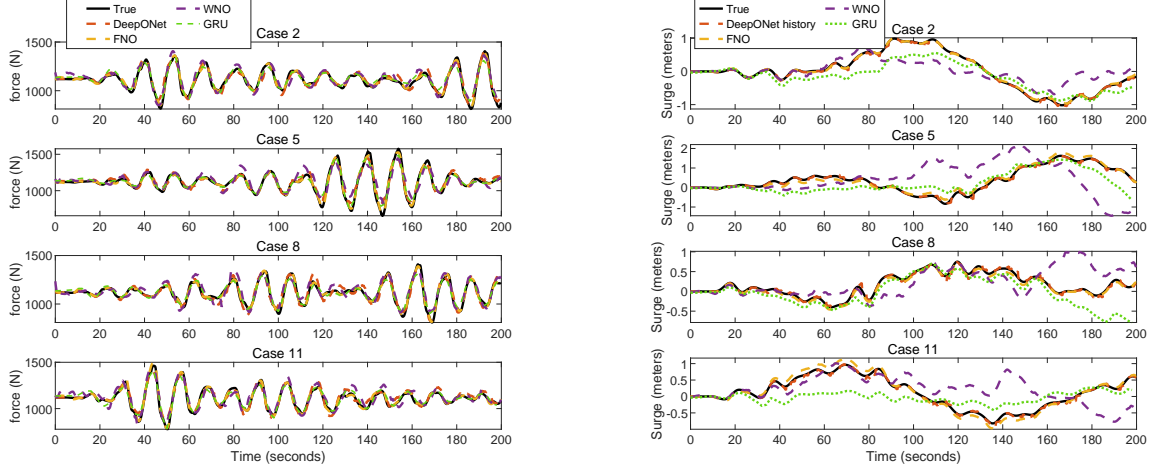


Fig. A.14: Comparison of the top tension of mooring #1 and surge response predictions obtained by the four models against the ground truth in Case 3. The plots on left show the top tension, while the plots on right show the surge motion.

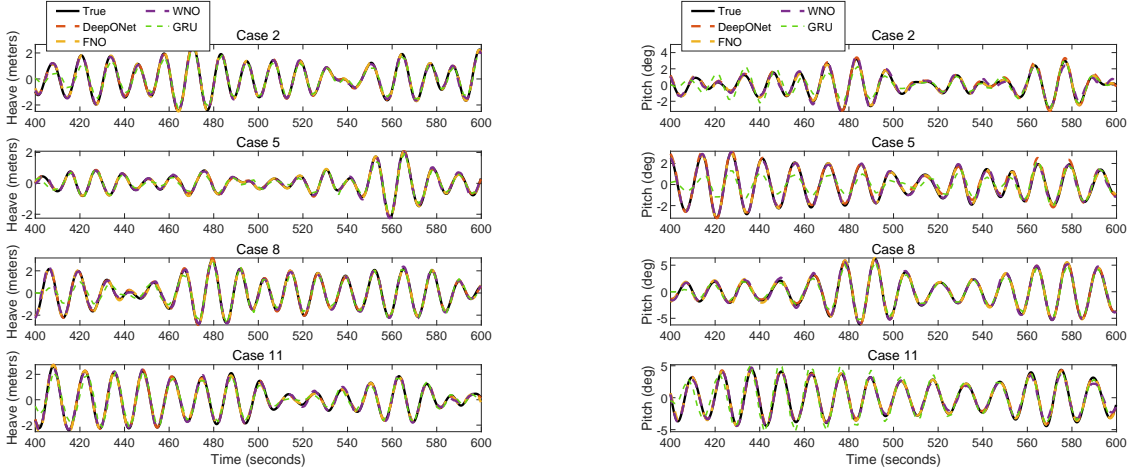


Fig. A.15: Comparison of heave and pitch responses predicted by the four models, DeepONet, FNO, WNO and GRU against the ground truth in Case 8. The plots on left show the heave motion, while the plots on right show the pitch motion.

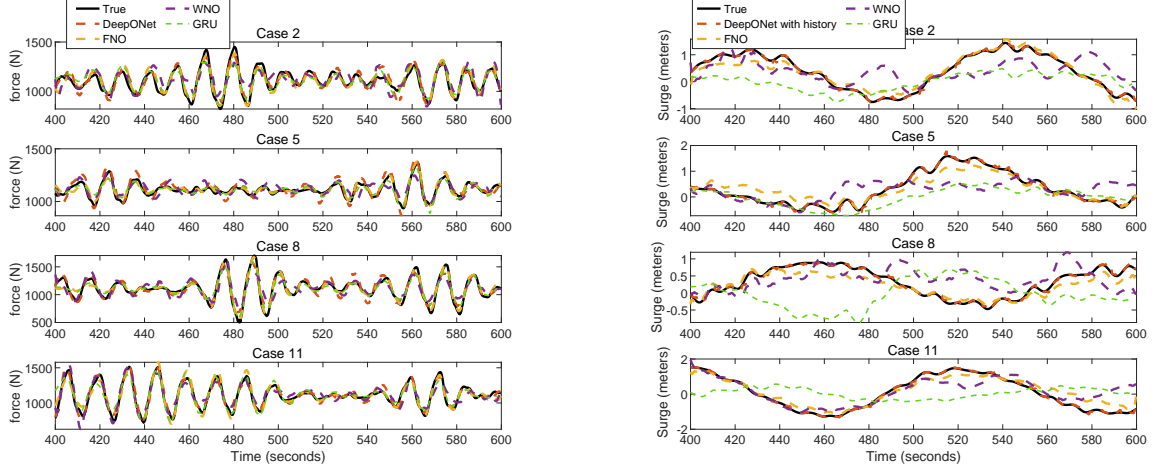


Fig. A.16: Comparison of the top tension of mooring #1 and surge response predictions obtained by the four models against the ground truth in Case 8. The plots on left show the top tension, while the plots on right show the surge motion.

Appendix B. Mean and standard deviation of MSE

To evaluate the performance of the model, we compute the mean square error of the predictions, and we report the mean and standard deviation of this metric based on three independent training trials.

Table B.1: Mean Square error of predicted surge by operator networks with different initial conditions

Methods	Case 1		Case 2		Case 3		Case 4		Case 5	
	Mean	Std								
Vanilla DeepONet	2.87e-2	3.04e-3	3.16e-2	3.27e-3	2.99e-1	4.73e-3	1.14e-1	6.66e-3	9.91e-2	5.06e-3
POD-DeepONet	1.50e-2	1.99e-3	3.26e-2	4.57e-3	1.32e-1	8.08e-3	7.38e-2	2.32e-2	3.58e-2	3.82e-3
DeepONet with history	4.43e-4	2.43e-4	2.00e-3	8.56e-4	1.55e-3	9.07e-5	9.91e-4	3.76e-5	7.32e-4	1.19e-4
SA-DeepONet	2.00e-2	4.93e-4	2.80e-2	1.94e-2	7.43e-2	1.13e-2	9.18e-3	7.16e-4	8.34e-3	1.74e-3
W-DeepONet	2.43e-2	1.76e-3	8.43e-3	5.15e-4	2.91e-1	3.59e-2	8.16e-3	9.15e-4	6.07e-3	6.50e-4
FNO	3.39e-3	9.54e-5	5.03e-4	4.79e-5	9.36e-3	1.31e-3	3.11e-3	2.17e-4	1.93e-3	5.13e-5
WNO	3.65e-2	1.17e-3	1.07e-1	4.00e-3	1.81e-1	1.73e-2	2.36e-2	4.36e-4	1.68e-2	7.09e-4
SA-WNO	1.49e-2	1.53e-4	1.03e-2	2.06e-3	3.97e-2	1.13e-3	8.83e-3	7.45e-4	8.06e-3	5.12e-4
GRU	2.69e-3	4.04e-5	7.42e-2	2.65e-4	4.24e-1	1.15e-3	1.73e-1	1.15e-3	5.07e-2	2.08e-4
Case 6		Case 7		Case 8		Case 9		Case 10		
DeepONet history	Mean	Std								
	3.22e-3	4.89e-4	6.31e-2	1.50e-3	1.80e-3	5.89e-4	1.27e-3	1.32e-4	1.22e-3	2.52e-5
W-DeepONet	4.15e-2	3.03e-3	6.55e-2	6.18e-3	3.43e-1	2.46e-2	5.92e-2	1.31e-3	3.75e-2	5.97e-3
FNO	3.14e-2	5.60e-3	7.72e-2	5.22e-3	9.55e-2	4.73e-4	3.98e-2	4.88e-4	1.08e-3	2.98e-4
WNO	1.39e-1	1.04e-2	4.40e-1	2.52e-3	3.74e-1	6.43e-3	1.35e-1	2.15e-2	1.23e-1	1.74e-2
SA-WNO	6.22e-2	6.21e-3	1.05e-1	1.27e-2	3.30e-1	1.42e-2	5.87e-2	4.60e-3	4.98e-2	3.61e-3
GRU	1.57e-1	7.64e-3	4.29e-1	1.74e-2	4.23e-1	6.00e-3	3.57e-1	3.06e-3	2.99e-1	4.62e-2

Appendix C. Network architectures

Table C.1: Hyperparameters used in the DeepONet model for training an operator to approximate the degrees of freedom considering zero initial conditions of displacement and velocities.

Sea state	Response	Model	NN depth	NN width	Modes	Activation function	Learning rate	Iterations
All cases	Heave	vanilla DeepONet	3	100	/	sin	1e-4	100,000
All cases	Pitch	vanilla DeepONet	3	100	/	sin	1e-4	100,000
All cases	Tension	vanilla DeepONet	4	256	/	sin	1e-4	400,000

Table C.2: Hyperparameters used in the FNO for training an operator to approximate the degrees of freedom considering zero initial conditions of displacement and velocities.

Sea states	Response	Fourier layer	NN width	Modes	Activation function	Learning rate	Epochs
All cases	Heave Pitch Tension	4	32	50	ReLU	1e-3	300

Table C.3: Hyperparameters used in the WNO for training an operator to approximate the degrees of freedom considering zero initial conditions of displacement and velocities.

Sea states	Response	Mother Wavelet	Level	Layer	NN width	Activation function	Learning rate	Epochs
All cases	Heave Pitch Tension	db20	6	4	64	ReLU	1e-3	300

Table C.4: Hyperparameters of the GRU with zero initial conditions

Sea state	Response	Number of hidden layer	NN width	Number of dense layer	Learning rate	Iterations
Case 1	Heave Pitch Tension	1	50	1	1e-4	3,000
Case 2	Heave Pitch Tension	2	200	1	1e-4	3,000
Case 3	Heave Pitch Tension	2	200	1	1e-5	1,000

Table C.5: Hyperparameters used in the model for training a DeepONet to approximate the surge for considering zero initial conditions of displacement and velocities.

Model	Branch net	Trunk net	Activation	Learning function	Iterations rate	Others
Vanilla DeepONet	[750, 750, 750, 750]	[750, 750, 750, 750]	sin	1e-4	100,000	/
POD-DeepONet	[750, 750, 750, 100]	[750, 750, 750, 100]	sin	vary lr	1,000,000	/
DeepONet with history	[100, 100, 300]	[100, 100, 300]	sin	vary lr	100,000	5
SA-DeepONet	[512, 512, 512, 512]	[512, 512, 512, 512]	sin	vary lr	1,000,000	/
W-DeepONet	[128, 128, 128, 300]	[128, 128, 300]	sin	vary lr	1,000,000	db1(Mother wavelet)

Table C.6: Hyperparameters used in the model for training an operator to approximate the surge for considering zero initial conditions of displacement and velocities.

Model	Depth	Width	Modes	Activation function	Learning rate	Epochs	Others
FNO	4	32	501	ReLU	1e-3	300	/
WNO	4	64	6 (level of wavelet tree)	ReLU	1e-3	300	db20 (Mother wavelet)
SA-WNO	4	48	6 (level of wavelet tree)	GELU	1e-3	300	db24 (Mother wavelet)
GRU (Case 1)	1	50	/		1e-4	3,000	/
GRU (Case 2)	2	200	/		1e-4	3,000	/
GRU (Case 3)	2	200	/		1e-5	1,000	/
GRU (Case 4)	2	200	/		1e-5	1,000	/
GRU (Case 5)	2	200	/		1e-5	1,000	/

Table C.7: Hyperparameters used in the model for training a DeepONet to approximate the surge for considering different initial conditions of displacement and velocities.

Model	Branch net	Trunk net	Activation function	Learning rate	Iterations	Others
DeepONet with history (Cases 6/8-10)	[100,100,300]	[100,100,300]	sin	vary lr	100,000	5 steps
DeepONet with history (Case 7)	[100,100, 100, 100]	[100,100,100]	sin	vary lr	100,000	5 steps
W-DeepONet(Case 6)	[128, 128, 128, 128]	[128, 128, 128]	sin	vary lr	1,000,000	db1 (Mother wavelet)
W-DeepONet(Cases 7/9)	[128, 128, 128, 800]	[128, 128, 800]	sin	vary lr	1,000,000	db1 (Mother wavelet)
W-DeepONet(Case 8)	[128, 128, 128, 500]	[128, 128, 500]	sin	vary lr	1,000,000	db1 (Mother wavelet)
W-DeepONet(Case 10)	[256, 256, 256, 800]	[256, 256, 800]	sin	vary lr	1,000,000	db1 (Mother wavelet)

Table C.8: Hyperparameters used in the model for training an operator to approximate the surge for considering different initial conditions of displacement and velocities.

Model	Depth	Width	Modes	Activation function	Learning rate	Epochs	Others
FNO	4	32	501	ReLU	1e-3	300	/
WNO	4	64	6 (level of wavelet tree)	ReLU	1e-3	300	db20 (Mother wavelet)
SA-WNO	4	32	6 (level of wavelet tree)	GELU	1e-3	300	db24 (Mother wavelet)
GRU (Case 6)	1	50	/		1e-4	3,000	/
GRU (Case 7)	2	200	/		1e-4	3,000	/
GRU (Case 8)	2	200	/		1e-5	1,000	/
GRU (Case 9)	2	200	/		1e-5	1,000	/
GRU (Case 10)	2	200	/		1e-5	1,000	/